Advanced Battery Management Systems: Modeling and Numerical Simulation for Control

Seong Beom Lee, Raghav S. Thiagarajan, Venkat R. Subramanian[*], Simona Onori[*], *Senior Member, IEEE*

Abstract— **Battery management systems (BMSs) rely on empirical models, in the form of equivalent circuit models, thanks to their mathematical simplicity and low computational burden. However, empirical models undergo extensive calibration efforts, and they lack in transferability across chemistries. In addition, the inability to predict electrochemical internal states and account for degradation dynamics usually lead to ill usability of the battery system, possibly resulting in inaccurate state of health (SOH) estimations diverging over time. An advanced BMS design that can observe, and control internal variables of the battery system is imperative to overcome these limitations, enabling long-lasting, safer, and cost-effective battery systems for the fast-growing energy market. Physics-based battery models have been regarded as one of the appropriate modeling frameworks to be integrated into the next-generation BMS. In model-based estimation, available input/output sensor information (e.g., current, voltage, and temperature) are used along with a mathematical representation of the battery dynamics to estimate the internal states. The purpose of this tutorial paper is to review implementation challenges of physics-based battery models and provides an overview of the latest research trends focusing on numerical algorithms and observer designs for hardware implementation of physics-based battery models towards the advanced BMS.**

I. INTRODUCTION

Lithium-ion batteries are currently the most popular electrochemical energy storage system to support and operate renewable energy applications and electric vehicles (EVs) thanks to their high specific power (300-1,500W/kg) and specific energy (100-270Wh/kg) [7, 8]. The battery system configuration is typically hierarchized from a cell level to a module and a pack level.

A lithium-ion cell is a basic unit of a lithium-ion battery containing a cathode, a separator, and an anode. The lithium-ion cell system includes components at both the micro- and macro-scale. Micro-scale components represent the solid particles in the cathode and anode, whereas the macro-scale one consists of the electrolyte across the cathode, separator, and anode. In a lithium-ion cell system, electrons flow through an external circuit from the anode to the cathode (or from the cathode to the anode), while ions in the electrolyte are transported through the separator [1, 9, 10]. The battery module is a battery assembly that thermally interacts with individual cells by packing them closely together. The heat transfer through conduction between the surface of neighboring cells is one of the key factors to causing different aging trajectories of individual cells in a module [5, 9, 12]. The battery pack is the final shape of the battery system installed in system-level applications, such as power grid and sustainable transport. It consists of battery modules connected in series and parallel, typically mounted on a system platform to provide the power and energy needed for the targeted application [14]. Lithium-ion battery packs always rely on a battery management system (BMS) to operate in a safe and efficient way, to achieve the desired performance while guaranteeing longevity of the pack. Typically, the current BMS employs an onboard microcontroller unit for capturing data from sensors through its peripherals as well as processing the data to make appropriate decisions and an analog front end for sensing signals from battery systems [16].

Mathematical battery models are typically used to understand, predict, control, and optimize battery performance in the BMS. The accuracy of BMS estimates largely depends on the accuracy and fidelity of the battery model used. By implementing adequate battery models, the viability and cost-effectiveness of existing electrochemical energy storage technologies used for transportation and grid storage can be further enhanced [17]. However, battery models must be implemented in low-cost BMS hardware components to make it commercially viable. This constrains the use of complex models in the BMS due to their memory and computational power needs, necessitating costly hardware. For this reason, the current practice employs empirical models, consisting of simple electric circuit components in the BMS thanks to their low computational cost and straightforward implementation [39]. However, empirical models are limited in providing physical insights and accurate aging predictions without vast amounts of testing and validation. Their accuracy varies with the calibration effort that goes to design accurate empirical models and chemistry specific [15]. The growing market of lithium-ion batteries in consumer electronics, automobiles, unmanned aerial vehicles, and the power grid sector has stressed the need and relevance for a properly designed advanced BMS that can ensure the battery system's reliability and performance.
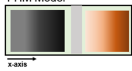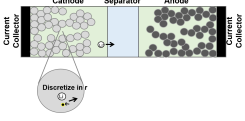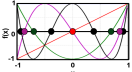
An advanced BMS that can monitor and optimize battery behavior and predict internal electro-mechanical/chemical states and guarantee safety is essential

S. B. Lee is with the Department of Energy Resources Engineering, Stanford University, Stanford, CA 94305 USA (email: sblee3487@gmail.com).

R. S. Thiagarajan is with the Department of Mechanical Engineering, the University of Texas, Austin, TX 78712 USA (e-mail: raghave.thiagarajan@utexas.edu).

V. R. Subramanian is with the Department of Mechanical Engineering, the University of Texas, Austin, TX 78712 USA (e-mail: venkat.subramanian@utexas.edu).

S. Onori is with Department of Energy Resources Engineering, Stanford University, Stanford, CA 94305 USA (e-mail: sonori@stanford.edu).
[*]Corresponding authors

Table I. Challenges and selected research trends towards advanced BMSs

Implementation Issue	Research approaches	Comments	Ref.
High computational burden: *Internal characteristics of the pseudo-two-dimensional axis cause expensive computational cost*	(i) Alternative modeling tool: full homogenized model	· Consumes 60% of the computational costs over the DFN model. · Exhibits a decreased RMSE up to 75% over the DFN model under medium-high temperature EV operating conditions	[3, 4]
	(ii) Mathematical reformulation of the DFN model	· Orthogonal collocation and polynomial and biquadratic approximation for the solid phase concentration (milli-second scale simulation) · Coupled with real-time nonlinear model predictive control (NMPC)	[1, 5, 6]
	(iii) Reduced order models from the DFN model	· An optimal observer design was proposed coupling with reduced-order models	[10, 11]
Initialization: *In the DAE system, AEs act as constraints, and consistent initial conditions are not known priori*	Single-step iteration-free initialization for the DAE system	· The DFN model has been simulated with this initialization approach in the Maple environment	[13]
Optimal parameter identification	Robust and sleek MATLAB$^{®}$ framework	· Efficiently enables to couple various optimization techniques with the DFN model relying on the single-step iteration-free initialization approach	[15]

in renewable grid and EV systems. Model-based estimation uses available input/output sensor information (current, voltage, and temperature) to predict the internal battery states. It is key to know the values of these internal parameters to facilitate the application of control principles-e.g., to develop efficient charging/discharging profiles [1, 6]. Physics-based models are considered an adequate modeling tool for the next generation BMS applications. They can deliver high physical interpretability of internal electrochemical states, which can be used to maximize the safety, usability, and lifetime of the battery system. Therefore, the model choice has currently gravitated from empirical models towards physics-based electrochemical models capable of capturing the battery behavior and degradation accurately, as they describe the internal dynamics of the battery and retain relevant physics for precise state estimation.

Physics-based models have been implemented in combination with degradation mechanisms, including the solid electrolyte interface (SEI) layer growth and lithium plating [18]. In lithium-ion batteries, for example, lithium plating can lead to an internal short circuit by piercing the separator with irregular dendrite-shaped growth, possibly causing the battery to catch on fire. If detailed information on lithium plating near a separator is obtained, thermal runaway can be avoided by safer battery operation. Additionally, knowledge of the internal states can be used to minimize plating side reactions by controlling overpotential. Mathematically, lithium plating occurs when the anode overpotential is negative, and it can be minimized by restricting the overpotential above zero in the physics-based modeling framework. The Doyle-Fuller-Newman (DFN) model is currently the most popular physics-based model used by the battery community to predict the electrochemical dynamics of lithium-ion batteries. The DFN model is made of partial differential equations (PDEs), which are numerically discretized into a large set of ordinary differential equations (ODEs) and algebraic equations (AEs) for implementation

purposes [19]. There have been several challenges in implementing the physics-based model under the limited computational power and memory provided by onboard BMS hardware- e.g., computational costs, inconsistent initialization, and parameterization issues. Although the DFN model was developed in the late 1990s, an onboard physics-based model BMS has not yet been commercialized. However, strides in the direction of having advanced BMS close to commercialization have been made over the past decade thanks to advancements in numerical algorithms and control designs to alleviate these obstacles (*see Table I*) [6, 11]. The main objectives of this tutorial paper are to (i) provide a comprehensive summary of modeling frameworks and their pros and cons for estimation in battery systems, (ii) discuss challenges and opportunities in numerical algorithms for physics-based models, (iii) provide an exposure to the state-of-the-art technology in battery observability analysis and observer design, and (iv) present a robust DFN modeling implementation for inconsistent initial conditions within a co-simulation framework for parameter identification.

II. BATTERY MODELS

Battery modeling candidates for the advanced BMS can be data-driven and physics-based models.

Recent developments in data-driven models with machine learning (ML) techniques have gained considerable attention as tools for predicting battery performance [20-22], due to their potential to achieve high accuracy with low computational cost (e.g., millisecond-scale simulation). However, ML models, typically viewed as a black box, rely on extensive historical field data to achieve better accuracy. A massive amount of data over a population of fleets is needed in order to cover as many usage scenarios as possible and provide accurate predictions [23]. Lab data is often utilized to establish the data-driven approach, which may misrepresent battery aging under real-world operations, limiting the extension of data-driven models [15].

On the other hand, physics-based battery models have been considered one of the front-runner modeling candidates for the advanced BMS in the current battery community. The main advantage of physics-based models is that they can be simulated in real-time using efficient numerical algorithms as well as providing high physical interpretability of internal electrochemical states. In addition, physics-based models can integrate degradation mechanisms -*e.g., lithium plating* and be used to optimize fast charge and battery life while minimizing the growth of plated lithium. For example, lithium plating is known to occur during high charge C-rates and/or low-temperature operation. In physics-based modeling frameworks, the overpotential condition can be restricted above zero to identify optimal charging strategies, maximizing usability, performance, and life of the battery systems [1, 6].

B. DFN Model

DFN model is the most widely accepted physics-based model to predict electrochemical dynamics of lithium-ion batteries by the battery community [19]. The solid and the electrolyte phases are considered in the DFN model. In the solid phase, states evolve in the *x* and *r* dimension. In the electrolyte, states evolve in the *x* dimension only. The model predicts the evolution of lithium concentration in the solid phase $c_{s,i}(x, r, t)$, at the anode and at the cathode (*i=negative, positive*) the electrolyte concentration $c_e(x, t)$, solid phase potential $\phi_{s,i}(x, t)$, electrolyte electric potential, $\phi_e(x, t)$ (lithium-ion diffusion creates voltage gradients in both the electrodes and electrolyte), and lithium intercalation current J_i. The Butler-Volmer equation is used to describe the relationship between the lithium intercalation current and the overpotential. The difference between solid and electrolyte phase potentials drives the main intercalation reaction on both electrodes as well as a side reaction on the anode, - *e.g.,* leading to SEI layer growth [19]. All equations, variables, and parameters are shown in Tables II, III, IV, and V. In Table III, Equations 1, 5, and 7 represent electrolyte dynamics in the positive electrode, separator, and negative electrode, respectively. The electrolyte potential is represented by Equations 2, 6, and 8 in Table III. Equations 3 and 9 (Table III) represent solid particle potentials, and Equations 4 and 10 (Table III) represent solid particle concentrations. Additional equations related to governing equations are given in Table IV.

Table II. List of variables for DFN model

Symbol	Variables	Units
C	Electrolyte concentration	mol/m^3
c_s	Solid phase concentration	mol/m^3
Φ_1	Solid phase potential	V
Φ_2	Liquid phase potential	V
I	Applied current density	A/m^2
U_i	Open circuit potential at positive and negative	V
J_i	Pore wall flux at positive and negative	mol/m^2/s
Θ_i	State of charge at positive and negative	-

Table III. Governing equations for DFN model
Governing equations

Positive
$$\varepsilon_p \frac{\partial c}{\partial t} = \frac{\partial}{\partial x}\left(D_{eff,p}\frac{\partial c}{\partial x}\right) + a_p(1 - t_+)j_p \tag{1}$$

$$-\sigma_{eff,p}\frac{\partial \Phi_1}{\partial x} - \kappa_{eff,p}\frac{\partial \Phi_2}{\partial x} + \frac{2\kappa_{eff,p}RT}{F}(1 - t_+)\frac{\partial \ln c}{\partial x} = i_{app} \tag{2}$$

$$\frac{\partial}{\partial x}\left(\sigma_{eff,p}\frac{\partial \Phi_1}{\partial x}\right) = a_p F j_p \tag{3}$$

$$\frac{\partial c_{s,p}}{\partial t} = -\frac{1}{r^2}\left(\frac{\partial}{\partial r}D_{s,p}\left(\frac{\partial c_{s,p}}{\partial r}\right)\right) \tag{4}$$

Separator
$$\varepsilon_s \frac{\partial c}{\partial t} = \frac{\partial}{\partial x}\left(D_{eff,s}\frac{\partial c}{\partial x}\right) \tag{5}$$

$$-\kappa_{eff,s}\frac{\partial \Phi_2}{\partial x} + \frac{2\kappa_{eff,s}RT}{F}(1 - t_+)\frac{\partial \ln c}{\partial x} = i_{app} \tag{6}$$

Negative electrode
$$\varepsilon_n \frac{\partial c}{\partial t} = \frac{\partial}{\partial x}\left(D_{eff,n}\frac{\partial c}{\partial x}\right) + a_n(1 - t_+)j_n \tag{7}$$

$$-\sigma_{eff,n}\frac{\partial \Phi_1}{\partial t} - \kappa_{eff,n}\frac{\partial \Phi_2}{\partial x} + \frac{2\kappa_{eff,n}RT}{F}(1 - t_+)\frac{\partial \ln c}{\partial x} = i_{app} \tag{8}$$

$$\frac{\partial}{\partial x}\left(\sigma_{eff,n}\frac{\partial \Phi_1}{\partial x}\right) = a_n F j_n \tag{9}$$

$$\frac{\partial c_{s,n}}{\partial t} = -\frac{1}{r^2}\left(\frac{\partial}{\partial r}D_{s,n}\left(\frac{\partial c_{s,n}}{\partial r}\right)\right) \tag{10}$$

Table IV. Additional equations for DFN model

$$D_{eff,i} = D \cdot \varepsilon_i{}^{brugg}, \quad i = p, s, n \tag{11}$$

$$\sigma_{eff,i} = \sigma_i(1 - \varepsilon_i), \quad i = p, s, n \tag{12}$$

$$a_i = \frac{3}{R_i}(1 - \varepsilon_i), \quad i = p, n \tag{13}$$

$$j_p = 2c^{0.5}k_p c_{sp,surf}(c_{sp,max} - c_{sp,surf})^{0.5}\sinh\left(\frac{\alpha F}{RT}(\Phi_1 - \Phi_2 - U_p)\right) \tag{14}$$

$$j_n = 2c^{0.5}k_n c_{sn,surf}(c_{sn,max} - c_{sn,surf})^{0.5}\sinh\left(\frac{\alpha F}{RT}(\Phi_1 - \Phi_2 - U_n)\right) \tag{15}$$

Table V. A. Parameters for DFN model

Symbol	Parameter
σ_i	Solid phase conductivity ($i = p, n$)
ε_i	Porosity ($i = p, s, n$)
Brugg	Bruggeman coefficient
D	Electrolyte diffusivity
$D_{s,i}$	Solid phase diffusivity ($i = p, n$)
k_i	Reaction rate constant ($i = p, n$)
$c_{s,i,max}$	Maximum Solid phase concentration ($i = p, n$)
$R_{p,i}$	Particle radius ($i = p, n$)
a_i	Particle surface area to volume ($i = p, n$)
l_i	Region thickness ($i = p, s, n$)
t_+	Transference number
F	Faraday's constant
R	Gas constant
T	Temperature
α	Transfer coefficient
A_{cell}	Electrode area
c	Electrolyte concentration

III. NUMERICAL ALGORITHMS/MODELING APPROACHES TOWARDS ADVANCED BMS DESIGN

As part of the implementation process, the PDE system of the DFN model is converted to the differential algebraic equation (DAE) system by numerical discretization, resulting in ordinary differential equations (ODEs) (*see Equation 16*) and algebraic equations (AEs) (*see Equation 17*) as follows:

ODE: $\quad \dfrac{dy(t)}{dt} = \boldsymbol{f}(t, \boldsymbol{y}, \boldsymbol{z}),$ (16)

AE: $\quad \boldsymbol{g}(t, \boldsymbol{y}, \boldsymbol{z}) = 0$ (17)

where $\boldsymbol{z}$ represents the set of discretized AE variables, including the solid and liquid phase potential, $\boldsymbol{y}$ represents the set of discretized ODE variables, including the electrolyte and solid phase concentration, and t represents simulation time.

A. High computational cost

The DFN model typically generates considerable numbers of discretized variables when utilizing conventional discretization methods, such as the finite difference method (FDM), the finite volume method (FVM), and the finite element method (FEM) (note: the Appendix section provides detailed information on numerical discretization methods).

These discretization methods convert time and space domains into time domains. Equations 1, 4, 5, 7, and 10 in Table III are converted into ODE systems, Equations 2, 3 6, 8, and 9 in Table III are converted into AE systems. In addition, the pseudo-two-dimensional nature of the DFN model generates a large set of ODEs and AEs, resulting in high computational cost; The DFN model assumes that solid particles in the positive and negative electrodes are distributed in one dimension along the *x-axis* of the electrolyte, and the solid-phase concentration of each solid particle is solved along the radius *r* dimension at a particular discretized point on the *x-axis* in the electrolyte.

Consider numerically discretizing the cathode, separator, and anode, using 20 node points. For the electrolyte and solid phase potential, the cathode produces a total of 40 AEs, and for the electrolyte concentration, it produces 20 ODEs.

The solid particle is also discretized with a number of 5 node points. The solid particles are placed at each discretized point along with the *x-axis* of the LIB, resulting in a total number of 100 ODEs, and a total of 160 DAEs for the cathode. The anode is also discretized in the same way resulting in 160 DAEs. The separator contains 20 node points, which yields a total of 40 DAEs, consisting of 20 ODEs for the electrolyte concentration and 20 AEs for the electrolyte potential. The solid phase concentration and potential are ignored since they do not exist in the separator. Therefore, the total number of DAEs of the full-order DFN model becomes 160 + 160 + 40 = 360. Given the large number of DAEs to be solved,
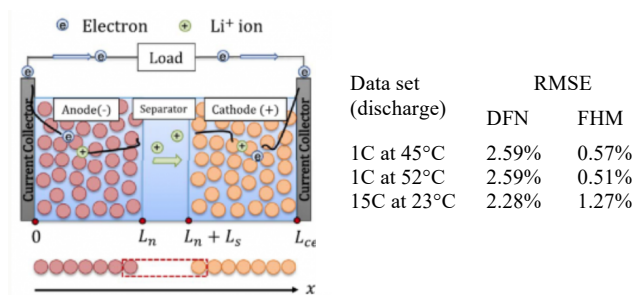

Data set (discharge)	RMSE	
	DFN	FHM
1C at 45°C	2.59%	0.57%
1C at 52°C	2.59%	0.51%
15C at 23°C	2.28%	1.27%

Figure 1. The electrochemical control-oriented model based on homogenization developed in 2015 provides higher accuracy in

simulation of the DFN model can be computationally expensive. This has been one of the main obstacles to incorporate the DFN model for advanced BMS design. The following sections A.1, A.2, and A.3 present modeling approaches and numerical algorithms to address the computational issues towards advanced BMS feasibility.

A-1. Alternative physics-based modeling tool

In references [3] and [4], the full homogenized macroscale (FHM) model was proposed as an alternative modeling framework to overcome the limitations of the DFN model (see, Figure 1). In the FHM framework, homogenization methods to upscale pore-scale battery dynamics are adopted to design a macroscale model of lithium-ion batteries [3, 4]. The FHM model is formulated under the assumption that the electrodes are composed of spatial unit cells, causing micro-scale continuity in the lithium-ion cell system. In addition, the FHM model's effective ionic properties are determined by resolving the closure problem in the unit cell of the electrode microstructure [3]. The FHM model also considers solid and electrolyte phases, *but the solid and electrolyte states evolve in the x dimension only*.

Reference [4] compares the performance of the DFN model with the FHM model in a COMSOL® environment adopting the FEM to numerically simulate battery models. Due to the one-dimensional implementation characteristic, the FHM model is reported to consume 60% of the computational costs over the DFN model under the same numerical discretization method. The FHM model predicts the evolution of average lithium concentration in the solid phase $\overline{c_{s,j}}(x, t)$, at the anode and at the cathode, average lithium concentration in the electrolyte $\overline{c_e}(x, t)$, average solid electric potential $\overline{\phi_{s,j}}(x, t)$, average electrolyte electric potential, $\overline{\phi_e}(x, t)$, and lithium intercalation current [4]. In addition to lower computational cost, the FHM model was reported to provide more accurate predictions over the low state of charge and medium-high temperature, as well as high C-rate (*see Figure 1*).

The DFN framework is based on the assumption that electrodes can be idealized as spherical-shaped particles. Moreover, simplifications are made to derive the effective coefficients for ionic diffusion and conductivity based on not-validated empirical laws. These assumptions possibly make the model ineffective and poor predictability leading to underutilization (or overutilization) of the battery system–and inaccuracy at the condition of operations in which electric vehicles would experience – e.g., low SOC, medium-high temperature, and medium-high C-rate. The FHM modeling framework exhibits a decreased root mean square error (RMSE) up to 75% when compared to the error generated from the DFN model under medium-high temperature conditions [4]. Despite the shortcomings of the DFN model under the aforementioned operating conditions, numerous studies have been conducted on capacity fade, mechanical stress effects, and several numerical approaches to implement the DFN model in advanced BMS applications its inception

in 1993. Thus, it is undeniable that the DFN model is currently the most used and understood modeling tool for advanced BMS, while the FHM model, which is still in the early stages of research, is also valuable as an alternative modeling framework.

A-2. Numerical algorithms for model predictive control

To maximize the battery system's usability and performance, models are required to be simulated in real-time. For example, charging/discharging optimization must be achieved within a given response time. Assume that the battery model consumes one millisecond to generate a single charge profile, and the response time is one second. In this scenario, a thousand different charging optimization protocols can be theoretically performed in one second. For this reason, identifying an optimal charging/discharging protocol is directly related to simulation speed because it determines how many different charging/discharging profiles can be generated to obtain the optimal profile within the given time framework [5, 6].

Several numerical approaches have been proposed to enable fast and efficient DFN model simulation. Mathematical reformulation of the DFN model is an efficient way of reducing the number of DAEs to improve the speed of simulation, thus enabling better control [5, 8]. This also lowers the memory footprint and allows for the use of economical hardware components in deploying the BMS.

The DFN model can be reformulated by making assumptions to simplify the physics or aggregating regions within a system, thereby reducing the number of equations to be solved.
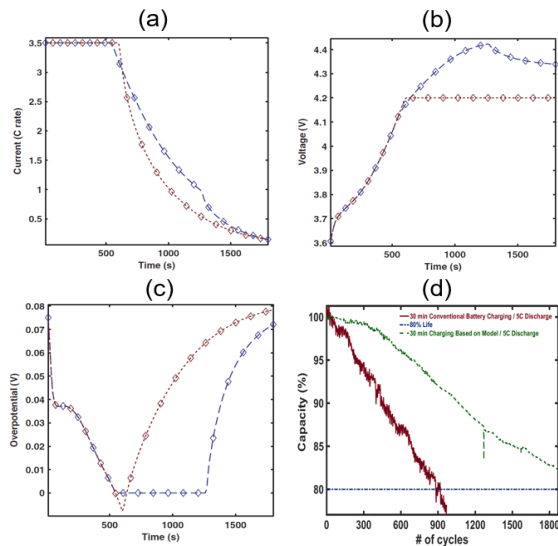

(a)   (b)

(c)   (d)

Figure 2. The fast charging protocol is validated with a 16Ah nickel-manganese-cobalt (NMC) pouch-type lithium-ion cell (3.5C rate as the upper limit for charging current) (a) optimal (long-dash) and CC-CV (short-dash) current-time curves (b) optimal (long-dash) and CC-CV (short-dash) voltage-time curves (c) optimal (long-dash) and CC-CV (short-dash) overpotential-time curves (d) optimal (short-dash) and CC-CV (straight line) cycling life [1]

Reference [8] proposed a polynomial and biquadratic approximation for the concentration profiles of lithium in the electrodes. Using such approximations reduces the number of equations to be solved and can be very efficient for long-time

scales. These approximations are ideal for adaptive solvers for the DFN model and have been shown to be accurate at low and medium charging/discharging C-rates of battery operation. Reference [5] used a coordinate transform for cathode-separator-anode units and adopted spectral methods such as orthogonal collocation combined with analytical solutions for electrochemical internal variables (*see comparison of single-discharge simulation time between the FDM and orthogonal collocation method in Table VI; more information related to orthogonal collocation can be found in the Appendix*).

Table VI. Comparison of DFN single-discharge simulation time between orthogonal collocation method and FDM [5]

Method	Number of DAEs	Simulation time (ms) [#]	RMSE (mV) [##]
FDM (50, 35, 50) [†]	590	4617	-
Collocation (1,1,1) [†]	20	46	17.84
Collocation (5,3,5) [†]	56	109	1.56

[†] Number of node point: (anode, separator, cathode)
[#] The simulation times are presented using a FORTRAN based DASSL solver
[##] RMSEs are calculated by difference between the FDM and collocation method

These reformulation techniques have recently been demonstrated to be used in optimal charging protocols [1, 6]. A significant push to adopt EVs over gasoline vehicles can come from reducing charging times by providing EVs with fast-charging capabilities. Since lithium plating is accelerated at high C-rates, it is critical to limit its formation while developing fast charging protocols. Reference [6] and [1] incorporate the DFN model via real-time nonlinear model predictive control (NMPC) to constrain the plating overpotential. A control formulation was proposed to maximize the charge stored such that the plating overpotential (anode overpotential) is greater than zero. Equations describing the same are shown below:

$$\max Q = \int_0^{t_f} i_{app}(t)dt \tag{18}$$

such that

$$0 < i_{app} < i_{max} \ (=3.5C)$$

$$\eta_{anode} > 0 \tag{19}$$

where Q is the charged stored in the battery, i_{app} is the applied charging current, t_f is the total time of charging, i_{max} is the maximum allowable current for charging, and $\eta_{plating}$ is the overpotential at the anode ($\Phi_1 - \Phi_2 - U_n$). Coupling this with a reformulated DFN model- a polynomial solid phase concentration approximation along with orthogonal collocation, a dynamic charging profile was designed in reference [1]. Figures 2(a) and 2(b) show the comparison of current and voltage profiles between NMPC and CC-CV charging protocol, respectively. It is seen that the cell voltage is higher in the former as the anode potential is being controlled to be constantly above zero, which prevents lithium plating, as can be seen from Figure 2(c). In Figure 2(d), the cycle life was reported to be more than doubled compared to standard CC-CV charging protocols [1]. The NMPC protocol has been applied to various cell types and chemistries and tested with experimental protocols to validate a longer cycling

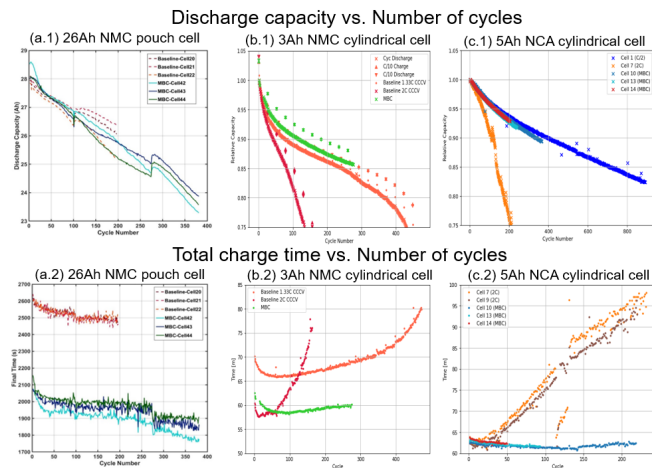life of the battery system (note: the data were provided by BattGenie, Inc).

Figure 3. (a) Optimal charging of a 26Ah pouch cell. (a.1) Discharge capacity vs cycle number is observed for baseline cells and optimally charged cells (a.2) Reduction in charging time is observed for optimally fast charged cells. Curves Model-based Control (MBC) - Cell42, MBC-Cell43 and MBC-Cell44 refers to the cells that are charged using the optimal charging profile. Baselines-Cell20/Cell21/Cell22 are charged using a baseline protocol. (b) Optimal charging of a 3Ah NMC 18650 cell using MBC. (b.1) MBC cell lasts for over 400 cycles compared to the baseline cell lasting 120 cycles before reaching End-of-Life (75% relative capacity). The orange ● refers to a baseline cell charged at 1.33 CC-CV (b.2) Clear reduction in charging time observed for optimally fast charged cell compared to the baseline cell. For comparison, the total charging time of a cell charged using a 1.33C CC-CV protocol is also plotted (orange ●). (c) MBC on a 5Ah NCA 21700 cell. Cells 10/13/14 (MBC) refer to the cells that are charged using the optimal charging profile. Cells 1/7/9 are charged using a baseline protocol, the C-rate used is mentioned in a bracket beside the cell number (example: Cell 7 is charged and discharged at 2C rate). (c.1) MBC cells have lost around 7% Relative Capacity compared to baseline Cell 7 that has lost 25% Relative capacity at cycle 200. (c.2) Clear reduction in charging time observed for optimally fast charged cells. MBC cells take around 62 minutes to charge compared to baseline Cell 7 and Cell 9, whose charging time increases with cycles from around 60 minutes at the start to 95 minutes after 200 cycles [2].

Fast charging of a 26Ah nickel-manganese-cobalt (NMC) pouch cell using model-based control shows a 23% reduction in the average charge time while compared to baseline cells (*see Figure 3a.1*), while achieving similar discharge capacity as the baseline cell (*see Fig 3a.2*). Experiments performed on a 3Ah NMC 18650 cell, being charged using an optimal charging profile have also shown significant improvements in battery performance. Figure 3b.1 depicts an improvement in cycle life by more than 200% (shown by green X) as compared to baseline 2C CC-CV protocol (shown by red X). Figure 3b.2 shows the total charging time of the cells using the baseline protocol and the optimal protocol. It is seen that using an optimal profile enables lower charging times of around 60 minutes for charging, while the baseline charge times for the 2C CC-CV profile increase from an initial time of 60 minutes to over 75 minutes after 150 cycles of operation. In addition,

model-based control on a 5Ah nickel-cobalt-aluminum (NCA) 21700 cell has shown improvement in cycle life (*see Figure 3c.1*) and achieved a faster charging time (*see Figure 3c.2*).

A-3. Reduced order models and observer design

Observability is defined as a structural property of the battery system that allows the internal state of a system to be inferred from available input and output sensor measurements [11]. In observable systems, therefore, an observer can be designed for the battery system, thereby estimating the internal state variables, including the SOC and SOH [11].

The mathematical structure of the DFN model has still been considered too complicated for observer implementation, even though the electrochemical model can account for electrochemical internal state variables [25]. Within the DFN modeling framework, therefore, additional assumptions have been added to construct reduced-order models with simplified descriptions of electrolyte dynamics and nonuniform reaction distributions, to help reduce the number of ODEs and AEs [15]. For example, the enhanced single particle model (ESPM) assumes that each electrode can be represented by a single spherical particle, which implies that all solid particles are uniform and have the same chemical properties. In the single particle model (SPM), the electrolyte dynamics is ignored [26, 38].

Observer design approaches have included model reduction and estimation. The first step towards creating a model-based observer is to verify the observability property of the model. For example, observability matrices have been used to check for local observability. Following observability analysis, the rank test of the observability matrix is applied to nonlinear battery modeling frameworks. A standard way of addressing nonlinear observability employs differential geometry to check the rank condition [11].

Studies on closed-loop observers and estimators for reduced-order electrochemical models have been extensively conducted to estimate internal states of a battery. A critical issue with observability in electrochemical models is the weak observability of lithium concentration when estimating solid-phase concentration in the positive and negative electrode separately. In order to overcome the weak observability, several methods to estimate the lithium concentration on a single electrode or both electrodes have been proposed in the literature such as single electrode observers, inclusion of thermal model and measurements, and interconnected observers [11].

Among many other observer designs (see, for example [25, 38, 39, 41]), reference [40] and [10] provide combined estimation of non-measurable critical battery variables such as lithium concentration and total cell capacity by using an electrochemical model-based interconnected observer (*see Figure 4*). Specifically, in [10] a dynamic relationship between capacity and power fade is exploited in order to formulate an adaptive interconnected observer by assuming that the SEI layer density is the dominant aging mechanism. By adopting a model-based adaptive interconnected observer, reference [10] proposes a real-time method to estimate lithium concentration in both electrodes, cell capacity, and

additional aging-sensitive parameters such as anode diffusion coefficient and ionic conductivity in the SEI layer. The capacity estimates were found to be within 2% of their respective true values across different lithium-ion cells in various states of health. Capacity estimates are also found to be robust against measurement noise and sensor bias as shown from the Battery-In-the-Loop validation performed on dSpace system [24].
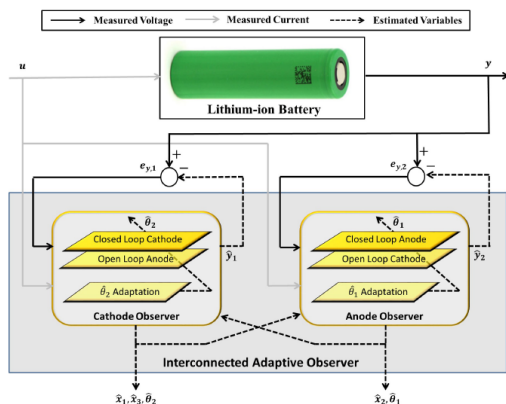

Figure 4. Interconnected adaptive observer structure for the estimation of lithium concentration states, total cell capacity, anode diffusion coefficient, and the SEI layer ionic conductivity .

B. Inconsistent initialization issue

In the DAE system, the definition of consistent initial conditions refers to initial values of y_0 and z_0 that satisfy the AE system (*see Equations 19*). In the DFN model, however, consistent initial conditions for all electrochemical variables are not known *a priori.* For this reason, the equilibrium state of the lithium-ion battery is used for initial guesses when implementing the DFN model. For example, initial guesses of solid-phase potentials at positive and negative electrodes are obtained from the values of positive and negative open-circuit potentials, respectively. Open-circuit potentials are a function of solid particle concentrations at the surface, and therefore, initial guesses of open-circuit potentials are determined by initial guesses of solid particle concentrations at the surface. The initial guesses of solid concentrations at the surface are given by the state of charge of the battery.

However, when the current is applied to the battery, the battery exits from its equilibrium state, and the aforementioned initial guesses no longer satisfy the AE constraint. The difference between initial guesses based on the equilibrium status and consistent ICs can be considerable, especially under high C-rate operating conditions. In addition, conventional numerical discretization methods, such as FDM, FVM, and FEM, generate many numbers of variables along with spatial scales at high number of node points. In this case, if inconsistent initial conditions are given, DAE solvers might not sort out the consistent initial conditions between the spatial variables. In order to determine consistent ICs, researchers have typically implemented iterative-based initialization approaches (e.g., *fsolve* and bisection algorithms); however, these iterative algorithms often come with fail to obtain consistent ICs [13].

B-1. Single-step iteration-free initialization approach

In 2015, a robust and efficient single-step iteration-free initialization approach was proposed to simulate the DAE system [13]. In the initialization approach, the DAE system is separated into AEs and ODEs. Next, while a switch function is multiplied by the ODEs, the AEs are converted into implicit ODE systems by the perturbation method [27]. In the final step, the implicit ODE system and the original ODE system including the switch function are simultaneously simulated. During a solving process, while implicit ODE systems identify the consistent initial conditions, the switch function converts the original ODEs into zero. Once consistent initial conditions are determined, the switch function is set to one. In this way, consistent initial conditions are guaranteed with a single-step iteration-free process. To date, the single-step iteration-free initialization approach has been implemented to simulate the DFN model in Maple® environment. A detailed derivation is described in the following paragraph.

AE system. AE variables are expressed as $g(t)$. When a perturbation parameter (ε) is a very small constant ($\ll 1$), $g(t')$ becomes zero as follows:

$$g(t') = \lim_{\varepsilon \to 0} g(t' + \varepsilon) = 0 \qquad (20)$$

When $t' = t + \varepsilon$, Equation 20 becomes

$$g(t + \varepsilon) = \lim_{\varepsilon \to 0} g(t' + 2\varepsilon) = 0 \qquad (21)$$

Therefore, from Equation 21,

$$g(t + \varepsilon) = 0 \qquad (22)$$

Equation 20 and Equation 22 have the relation as below.

$$g(t') = g(t + \varepsilon) = 0 \qquad (23)$$

The original AE to be solved is $g(t') = 0$. However, from Equation 23, solving $g(t + \varepsilon) = 0$ equals to solving $g(t') = 0$. By the Tayler series expansion,

$$g(t + \varepsilon) = g(t) + \varepsilon \frac{dg(t)}{dt} + \frac{1}{2}\varepsilon^2 \frac{d^2 g(t)}{dt^2} + \cdots \approx g(t) + \varepsilon \frac{dg(t)}{dt} \quad (24)$$

Combining Equation 23 with Equation 24,

$$\varepsilon \frac{dg(t)}{dt} - g(t) = 0 \qquad (25)$$

Arranging Equation 25,

$$\varepsilon \frac{dg(t)}{dt} = -g(t) \qquad (26)$$

We demonstrate that solving $g(t') = 0$ equals to solving $\varepsilon \frac{dg(t)}{dt} = -g(t)$ from Equations 20 to 26.

ODE system. ODE variables are expressed as $y(t)$. Equation 29 represents ODE systems.

$$\frac{dy(t)}{dt} = f(t, y, z) \qquad (27)$$

Now, a switch function is introduced.

$$T_H = \frac{1}{2}(1 + tanh\,(q(t - t_j)))\qquad(28)$$

If q has enough large values (e.g., 1000), switch function becomes zero when $t < t_j$ and becomes one when $t > t_j$. Now, Equation 27 is multiplied by Equation 28.

$$\frac{dy(t)}{dt} = f(t, y, z)\frac{1}{2}(1 + tanh\,(q(t - t_j)))\qquad(29)$$

This initialization approach combines Equation 26 and Equation 29 and solves AES and ODEs simultaneously. That is,

(i) when $t < t_j$, $\varepsilon\frac{dg(t)}{dt} = -g(t)$ will find consistent initial conditions

(ii) when $t > t_j$, $\frac{dy(t)}{dt} = f(t, y, z)$ and $\varepsilon\frac{dg(t)}{dt} = -g(t)$ are solved simultaneously.

B-2. MATLAB® framework and parameter identification

The initialization approach described in the previous section has recently been implemented in MATLAB®, one of the most widely used software in the control community. The DFN modeling framework was provided as an open-access MATLAB® code referred to as DEARLIBS (**D**oyle-Fuller-Newman **E**lectrochemical B**a**ttery Model Implementation in a **R**obust and Sleek MATLAB® Framework for **Li**thium-ion **B**atterie**s**), allowing users to simulate the DFN model along with a standard solver (e.g., *ode15s*) as well as identify model parameters directly after numerical discretization [15]. DEARLIBS adopts the FDM, over which the single-step iteration-free initialization approach is applied. The MATLAB® standard *ode15s* solver is then adopted as the solver of choice to simulate the DFN model. Kinetic/transport parameters of a commercial battery system (LG INR 21700) were identified at different temperatures (5°C, 25°C, and 35°C), adopting the particle swarm optimization (PSO) as an example of gradient-free optimization algorithms to minimize the RMSE between a 1C voltage discharging experimental profile and modeling voltage outputs (*see Figure 5*). In the PSO, a solution is represented by particles, including two vectors of position and velocity. Each particle moves to a new position using velocity based on the global best position in the PSO algorithm. When a new position is reached, the best positions of each particle are updated. Modeling voltage outputs were also validated with dynamic urban driving schedule profiles based on the identified parameters. In addition to robust and efficient initialization, DEARLIBS maximizes users' convenience, including a parameter identification routine along with a standard solver provided by MATLAB®. Currently, multiple parameters identification remains a challenge in the DFN model. The DFN model requires over 20 parameters to fully describe the physical, chemical, and electrochemical properties of LIBs. In commercial LIBs, model parameter values are generally not provided because battery manufacturers treat them as trade secrets.

Multiple parameters in the DFN model, such as geometric, kinetic, and transport parameters, can be mathematically identified simultaneously from available measurements of voltage, current, and temperatures. The multiple parameters identification techniques are essential to be used to update the transport and kinetic parameters of LIBs during battery operation. Current practice mostly focuses on fitting simulated voltage with experimental voltage data at different C-rates via a specific parameter identification algorithm. In DEARLIBS, a robust and efficient single-step iteration-free initialization algorithm is one of the most crucial parts to implement parameter identification techniques. A set of model parameter values are changed during the parameter identification process at every iteration. The iteration process requires different consistent initial conditions depending on a set of updated parameter values. The DEARLIBS simulates the DFN model using a standard solver, which enables users to efficiently couple and execute numerous parameter identification routines by relying on the Optimization Toolbox provided MATLAB®.
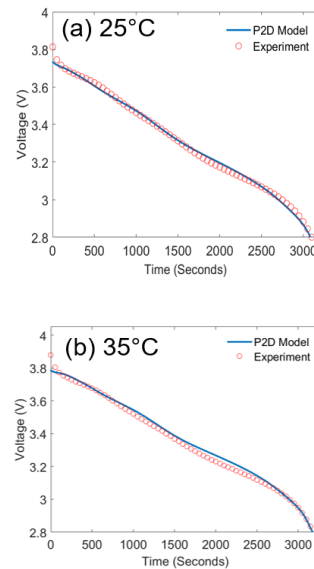

Figure 5. Comparison of voltage profiles between experimental data and battery model outputs from the DFN model. Voltage profiles from experimental measurement and DFN model outputs are compared at (a) 25°C and (b) 35°C (Experimental data: red-color and empty circle dots, the P2D model: blue-color straight line).

IV. CONCLUSION AND PERSPECTIVES

We discussed the necessity of a physics-based modeling framework for advanced BMS design. Challenges and research trends were introduced to address implementation issues, including high computational cost, inconsistent initialization, and parameter identification routines, as well as state observer design. One key challenge is to characterize and validate performance under different degradation stages occurring in lithium-ion battery systems. In physics-based modeling frameworks, a few main degradation mechanisms have been implemented -e.g., the SEI layer growth and lithium plating. Modeling degradation modes that occur in a battery throughout its lifespan is a massive undertaking as it requires coupling electrochemical, thermal, and mechanical effects at various length scales. Degradation mechanisms are coupled and nonlinear and they hard to observe through non-

invasive onboard BMS measurements. To address this issue, the concepts of several possible integration architectures for physics-based and data-driven models with machine learning techniques have been recently proposed to achieve better accuracy, robustness to limited or low-quality data, and life prediction generalizability. For this hybrid integration framework, historical operation data needs to be utilized for validation, but data storage is often limited in the onboard BMS [28, 29].

Cloud computing and the Internet of Things (IoT) can be leveraged to overcome onboard BMS limitations, providing high computation and data storage capability, as well as system reliability through wireless IoT communication [30]. New communication technologies such as 5G technology have led to an unprecedented increase in cloud adoption. 5G wireless technology delivers higher performance and improved efficiency through higher data speeds, low latency, more reliability, and massive network capacity empowering a new network of connectivity. These technologies together enable real-time monitoring, prediction, and fast optimization of battery systems with almost unlimited storage, processing capacity, and high system reliability. However, there are also concerns that the BMS should be the onboard system rather than the cloud-based control over battery operation. Cyberspace attacks are expected to proliferate with millions of connected sustainable transportation and renewable energy systems in the cloud environment. There is the possibility of catastrophic infrastructure disruption from cyberattacks such as malicious commands and incorrect over-the-air updates. Cybersecurity demands much attention and is critical in regulating malicious hacking [31, 32]. The state-of-the-art research technologies introduced in this paper unlock the potential to implement physics-based models that provide an information on internal electrochemical states in real-time and optimal fast charge strategies while minimizing memory, even when executing in an onboard BMS as well as a cloud environment. Implementing physics-based models can alleviate critical weaknesses of current BMS related to the inability to capture degradation mechanisms using empirical models. Through advanced BMS computing, we envision that battery performance and usability can be enhanced, providing longer and safer battery use.

APPENDIX

The finite difference method (FDM) is the most direct approach to discretizing the PDE system. In the FDM framework, a point on the *x-axis* (or *r-axis*) represented by the continuum representation of the governing equations is converted into a set of discrete equations. The FDM is considered the easiest and most straightforward discretization method while producing an accurate performance on regular geometries (e.g., one-dimensional setting and rectangular-shaped models) [33]. In the FDM, for example, time and space domains of the DFN model are converted into time domains at each local point; the first and second order *x*- and *r-derivatives* of PDEs are converted into ODEs as follows:

First order: $\frac{\partial Y_i(x,t)}{\partial x} = \frac{Y_{i+1}(t) - Y_i(t)}{h}$ (A.1)

$$\frac{\partial c_{i,j}(x,r)}{\partial r} = \frac{c_{i+1,j}(t) - c_{i,j}(t)}{h_r}$$ (A.2)

Second order: $\frac{\partial^2 Y_i(x,t)}{\partial x^2} = \frac{Y_{i+1}(t) - 2Y_{i+1}(t) + Y_{i-1}(t)}{h^2}$ (A.3)

$$\frac{\partial^2 c_{i,j}(x,t)}{\partial r^2} = \frac{c_{i+1,j}(t) - 2c_{i+1,j}(t) + c_{i-1,j}(t)}{h_r^2}$$ (A.4)

In the finite volume method (FVM), the differential form of the material balance is replaced with an integrated form [33]. Consider one-dimensional transport in the element shown in Fig. 1.A. At steady state, a shell mass balance is written as

$$\begin{Bmatrix} rate\ of \\ mass\ in \end{Bmatrix} - \begin{Bmatrix} rate\ of \\ mass\ out \end{Bmatrix} + \begin{Bmatrix} rate\ of \\ production \end{Bmatrix} = 0 \quad (A.5)$$
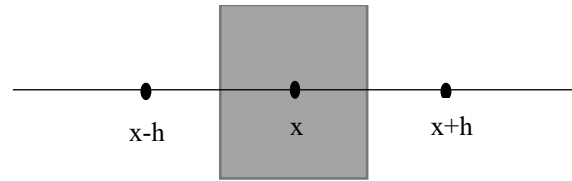

Figure 1.A. A control volume. Fluxes are evaluated at the faces between node points, and mass is rigorously conserved

or on a unit area basis,

$$N_A\left(x - \frac{h}{2}\right) - N_A\left(x + \frac{h}{2}\right) + R_A h = 0 \quad (A.6)$$

where N_A is the flux of species A, R_A is the homogenous production rate, and *h* is the thickness of the element.

Typically, after making the balance for a shell of finite thickness, one lets the thickness of the shell, *h*, become infinitesimally small. Performing this and substituting Fick's law for diffusion gives

$$\frac{d}{dx}\left(D_A \frac{dC_A}{dx}\right) + R_A \quad (A.7)$$

Equation A.7. is then cast in finite-difference form via a Taylor-series expansion, and the resulting algebraic equations are solved numerically. For the finite volume approach, instead of making the step size infinitesimally small, one works directly with A.6. The fluxes at $x \pm \frac{h}{2}$ are expressed with Fick's law and then cast in finite difference form. The main feature of the finite-volume formulation is the integral conservation of material, momentum etc. Since the fluxes in the common face between two adjacent control volumes are represented by the same expression, material is rigorously conserved. This

conservation is preserved regardless of the mesh size. In contrast, it can be shown that, when D_A is not constant, the standard finite-difference approximation of Equation A.7. conserves material only in the limit of h approaching zero [34]. The FVM divides the spatial axis domain in the PDE system into finite-sized elements of control volumes. The FVM is established by the integral conservation law on each of the control volumes where the flux entering a given volume is identical to leaving the adjacent volume. While FDM solves differential form, FVM is a general solution technique for uniform and un-structured grids since it solves the integral form. FVM handles better discontinuities in boundary conditions compared to FDM.

Figure 2.A describes the FVM coordinate and compares the FVM coordinate with the FDM coordinate [35]. For example, when the number of FDM internal nodes is 4, the number of FVM internal nodes is 5 (N′=5), and the FVM includes imiginary points beyond or before its boundaries (see Φ'_0 and Φ'_6). Likewise the FDM coordinate, the subscript i presents the ith order of nodes, but in the FVM coordinate, when N′=n, the value i ranges from 0 to n+1 (e.g., when n=5, i ranges from 0 to 6). The potential value on the ith node is expressed as Φ'_i and the value is located in the middle of Φ_{i-1} and Φ_{i+1} in the FDM coordinate. In the one-dimensional coordinate of the FVM, Φ'_i can be expressed as a function of $(\Phi'_{i-1} + \Phi'_{i+1})/2$. Also, the ith position of the coordinates can be expressed as $Y_i = h'_i/2 + Y_{i-1}$ ($Y_1 = h_1/2$). The first and second order x- and r-derivatives of PDEs in the FVM are converted into ODEs as follows:

First order: $\dfrac{\partial Y_i(x,t)}{\partial x} = \dfrac{Y_{i+1}(t) - Y_i(t)}{h'}$ (A.8)

$\dfrac{\partial c_{i,j}(x,r)}{\partial r} = \dfrac{c_{i+1,j}(t) - c_{i,j}(t)}{h_{r'}}$ (A.9)

Second order: $\dfrac{\partial^2 Y_i(x,t)}{\partial x^2} = \dfrac{Y_{i+1}(t) - 2Y_{i+1}(t) + Y_{i-1}(t)}{h'^2}$ (A.10)

$\dfrac{\partial^2 c_{i,j}(x,t)}{\partial r^2} = \dfrac{c_{i+1,j}(t) - 2c_{i+1,j}(t) + c_{i-1,j}(t)}{h_{r'}^2}$ (A.11)

Orthogonal collocation expands the solution of a desired variable in orthogonal polynomials in the *x* space dimension. When applied to porous electrode, the battery system is discretized in the x-direction while maintaining dependence of variables in the time domain to be solved by time-adaptive solvers. In the reformulation, the variable of interest is approximated by a summation of trial functions of the form as follows:

$u(X,t) = F(X,t) + \sum_{k=0}^{N} B_k(t) T_k(X)$ (A.12)

where $u(X,t)$ is the variable of interest, $T_k(X)$ are the chosen trial functions with homogenous boundary conditions, $F(X,t)$ is a function chosen to satisfy the time-dependent boundary conditions, and $B_k(t)$ are the coefficients of the trial functions. Note, the choice of the trial function does affect the accuracy of the final solution. This method has been adopted in reference [5] for galvanostatic boundary condition. The current density is approximated as a sum of polynomials using

orthogonal collocation which allowed to find an analytical solution for the solid-phase potential in the x dimension. This
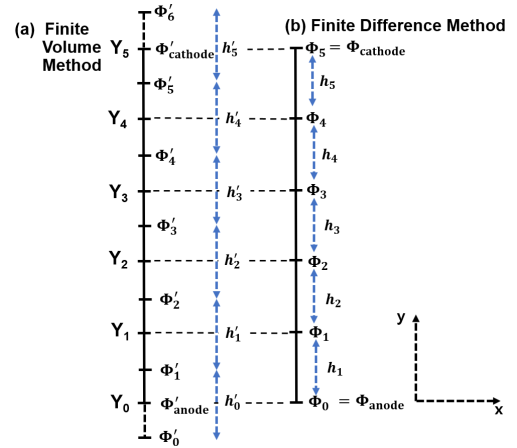

Figure 2.A. The comparison of the 1-D coordinate between finite difference and finite volume methods. The potential values (Φ_i and Φ'_i), the node spacing (h_i and h'_i), and the coordinate position (Y_i) are described on the 1-D coordinate of the finite difference and finite volume method. In the 1-D coordinate, potential profiles of Φ'_i in the FVM is located in the middle of Φ'_{i-1} and Φ'_{i+1} in the FDM, and the 1-D coordinate has the linear profile, Φ'_1 can be expressed as $(\Phi'_{i-1}$ and $\Phi'_{i+1})/2$. Therefore, can be calculated by $(\Phi'_0 + \Phi'_1)/2$.

allowed for a closed form solution for the solid-phase potential as a function of other dependent variables without compromising on accuracy. The same is done for all the dependent variables and suitable number of collocation points are chose which can reduce the number of DAEs [5]. Many spatial discretization methods exist, including the FDM (constant grid, variable grid, higher order), FVM, spectral methods, and global and local FEM (strong form and weak form). All these methods result in a system of algebraic equations for steady-state models, and a system of differential-algebraic equations (DAEs) for models with time dynamics. Some methods might be more suitable than others for certain problems. For example, the FEM in its weak form only conserves flux globally and not locally, whereas the finite volume formulation ensures that the flux is conserved locally in each finite volume considered. Higher order methods work very well for elliptic PDEs with no singularities, but for highly convective PDEs, a lower order locally conservative FVM may be more directly applicable. The best choice for spatial discretization can be answered by performing grid convergence studies [36]. Once the spatial discretization is chosen, the resulting set of DAEs can be integrated in time with adaptive solvers using Method of Lines (MOL). It should be noted that a particular spatial discretization approach providing a particular order of accuracy for steady-state models may not provide the same order of accuracy in a MOL framework. In addition, all the time-integrators will not provide the expected order of accuracy in temporal discretization for the numerical simulation of DAEs, in particular close to the boundaries, which are of interest for battery models. For example, while backward differential formula (BDF) methods can integrate stiff DAEs, the same approach, when used for temporal

discretization in a simultaneous approach framework, loses order of accuracy (and yields unstable results) even for simple ODEs [37].

REFERENCES

[1] M. Pathak, D. Sonawane, S. Santhanagopalan, R. D. Braatz, and V. R. Subramanian, "Analyzing and minimizing capacity fade through optimal model-based control-theory and experimental validation," *ECS transactions,* vol. 75, p. 51, 2017.

[2] BattGenie, Inc (2020) Available: https://battgenie.life/technology/

[3] H. Arunachalam, S. Onori, and I. Battiato, "On veracity of macroscopic lithium-ion battery models," *Journal of The Electrochemical Society,* vol. 162, p. A1940, 2015.

[4] H. Arunachalam and S. Onori, "Full homogenized macroscale model and pseudo-2-dimensional model for lithium-ion battery dynamics: comparative analysis, experimental verification and sensitivity analysis," *Journal of The Electrochemical Society,* vol. 166, p. A1380, 2019.

[5] P. W. Northrop, V. Ramadesigan, S. De, and V. R. Subramanian, "Coordinate transformation, orthogonal collocation, model reformulation and simulation of electrochemical-thermal behavior of lithium-ion battery stacks," *Journal of The Electrochemical Society,* vol. 158, p. A1461, 2011.

[6] S. Kolluri, S. V. Aduru, M. Pathak, R. D. Braatz, and V. R. Subramanian, "Real-time nonlinear model predictive control (NMPC) strategies using physics-based models for advanced lithium-ion battery management system (BMS)," *Journal of The Electrochemical Society,* vol. 167, p. 063505, 2020.

[7] S. Xia, X. Wu, Z. Zhang, Y. Cui, and W. Liu, "Practical challenges and future perspectives of all-solid-state lithium-metal batteries," *Chem,* vol. 5, pp. 753-785, 2019.

[8] V. R. Subramanian, V. D. Diwakar, and D. Tapriyal, "Efficient macro-micro scale coupled modeling of batteries," *Journal of The Electrochemical Society,* vol. 152, p. A2002, 2005.

[9] A. Allam and S. Onori, "Exploring the dependence of cell aging dynamics on thermal gradient in battery modules: A PDE-based time scale separation approach," in *2019 18th European Control Conference (ECC)*, 2019, pp. 2380-2385.

[10] A. Allam and S. Onori, "Online capacity estimation for lithium-ion battery cells via an electrochemical model-based adaptive interconnected observer," *IEEE Transactions on Control Systems Technology,* vol. 29, pp. 1636-1651, 2020.

[11] A. Allam and S. Onori, "Linearized Versus Nonlinear Observability Analysis for Lithium-Ion Battery Dynamics: Why Respecting the Nonlinearities Is Key for Proper Observer Design," *IEEE Access,* vol. 9, pp. 163431-163440, 2021.

[12] V. Azimi, A. Allam, W. T. Joe, Y. Choi, and S. Onori, "Fast Charging-Minimum Degradation Optimal Control of Series-Connected Battery Modules with DC/DC Bypass Converters," in *2021 American Control Conference (ACC)*, 2021, pp. 231-236.

[13] M. T. Lawder, V. Ramadesigan, B. Suthar, and V. R. Subramanian, "Extending explicit and linearly implicit ODE solvers for index-1 DAEs," *Computers & Chemical Engineering,* vol. 82, pp. 283-292, 2015.

[14] J. Li and M. S. Mazzola, "Accurate battery pack modeling for automotive applications," *Journal of Power Sources,* vol. 237, pp. 215-228, 2013.

[15] S. B. Lee and S. Onori, "A robust and sleek electrochemical battery model implementation: a MATLAB® framework," *Journal of The Electrochemical Society,* vol. 168, p. 090527, 2021.

[16] M. Akdere, M. Giegerich, M. Wenger, R. Schwarz, S. Koffel, T. Fühner*, et al.*, "Hardware and software framework for an open battery management system in safety-critical applications," in *IECON 2016-42nd Annual Conference of the IEEE Industrial Electronics Society*, 2016, pp. 5507-5512.

[17] S. B. Lee, C. Pathak, V. Ramadesigan, W. Gao, and V. R. Subramanian, "Direct, efficient, and real-time simulation of physics-based battery models for stand-alone pv-battery microgrids," *Journal of The Electrochemical Society,* vol. 164, p. E3026, 2017.

[18] G. Pozzato, S. B. Lee, and S. Onori, "Modeling degradation of Lithium-ion batteries for second-life applications: preliminary results," in *2021 IEEE Conference on Control Technology and Applications (CCTA)*, 2021, pp. 826-831.

[19] M. Doyle, T. F. Fuller, and J. Newman, "Modeling of galvanostatic charge and discharge of the lithium/polymer/insertion cell," *Journal of the Electrochemical society,* vol. 140, p. 1526, 1993.

[20] R. R. Richardson, C. R. Birkl, M. A. Osborne, and D. A. Howey, "Gaussian process regression for in situ capacity estimation of lithium-ion batteries," *IEEE Transactions on Industrial Informatics,* vol. 15, pp. 127-138, 2018.

[21] X. Hu, Y. Che, X. Lin, and S. Onori, "Battery health prediction using fusion-based feature selection and machine learning," *IEEE Transactions on Transportation Electrification,* vol. 7, pp. 382-398, 2020.

[22] D. Roman, S. Saxena, V. Robu, M. Pecht, and D. Flynn, "Machine learning pipeline for battery state-of-health estimation," *Nature Machine Intelligence,* vol. 3, pp. 447-456, 2021.

[23] L. Song, K. Zhang, T. Liang, X. Han, and Y. Zhang, "Intelligent state of health estimation for lithium-ion battery pack based on big data analysis," *Journal of Energy Storage,* vol. 32, p. 101836, 2020.

[24] A. Allam, E. Catenaro, S. Onori, "Pushing the Envelope in Battery Estimation Algorithms", *iScience*, Volume 23, Issue 12, 2020

[25] S. J. Moura, M. Krstic, and N. A. Chaturvedi, "Adaptive PDE observer for battery SOC/SOH estimation," in *Dynamic Systems and Control Conference*, 2012, pp. 101-110.

[26] V. Ramadesigan, P. W. Northrop, S. De, S. Santhanagopalan, R. D. Braatz, and V. R. Subramanian, "Modeling and simulation of lithium-ion batteries from a systems engineering perspective," *Journal of the electrochemical society,* vol. 159, p. R31, 2012.

[27] R. N. Methekar, V. Ramadesigan, J. C. Pirkle Jr, and V. R. Subramanian, "A perturbation approach for consistent initialization of index-1 explicit differential–algebraic equations arising from battery model simulations," *Computers & Chemical Engineering,* vol. 35, pp. 2227-2234, 2011.

[28] M. Aykol, C. B. Gopal, A. Anapolsky, P. K. Herring, B. van Vlijmen, M. D. Berliner*, et al.*, "Perspective—combining physics and machine learning to predict battery lifetime," *Journal of The Electrochemical Society,* vol. 168, p. 030525, 2021.

[29] J. Willard, X. Jia, S. Xu, M. Steinbach, and V. Kumar, "Integrating scientific knowledge with machine learning for engineering and environmental systems," *arXiv preprint arXiv:2003.04919,* 2020.

[30] W. Li, M. Rentemeister, J. Badeda, D. Jöst, D. Schulte, and D. U. Sauer, "Digital twin for battery systems: Cloud battery management system with online state-of-charge and state-of-health estimation," *Journal of Energy Storage,* vol. 30, p. 101557, 2020.

[31] S. Levine, "EV Hackers Are Coming-and a Fortune Awaits Their Foes, " The Electric (2021) Available: https://www.theinformation.com/newsletters/the-electric/archive/e50f17f0-acc0-43fc-9b43-6c323696faf1.

[32] R. Leventov, "Digital Twin for Battery Systems: Cloud BMS with Online State-of-Charge and State-of-Health Estimation, " Battery Discovery (2021) Available: https://batterydiscovery.substack.com/p/digital-twin-for-battery-systems.

[33] J. Peiró and S. Sherwin, "Finite difference, finite element and finite volume methods for partial differential equations," in *Handbook of materials modeling*, ed: Springer, 2005, pp. 2415-2446.

[34] C. Hirsch, "Numerical computation of internal & external flows: fundamentals of numerical discretization," *John Wiley & Sons, Inc.*, 1988.

[35] S. B. Lee, "Integrating Energy Storage Systems into Renewable Grid Applications: A Model-based Approach," *University of Washington*, 2019.

[36] K. Shah, A. Subramaniam, L. Mishra, T. Jang, M. Z. Bazant, R. D. Braatz*, et al.*, "Editors' Choice—Perspective—Challenges in Moving to Multiscale Battery Models: Where Electrochemistry Meets and Demands More from Math," *Journal of The Electrochemical Society,* vol. 167, p. 133501, 2020.

[37] W. W. Hager, "Rates of convergence for discrete approximations to unconstrained control problems," *SIAM Journal on Numerical Analysis,* vol. 13, pp. 449-472, 1976

[38] S. Santhanagopalan and R. E. White, ''State of charge estimation using an unscented filter for high power lithium ion cells,'' Int. J. Energy Res., vol. 34, no. 2, pp. 152–163, 2009.

[39] G. L. Plett, ''Extended Kalman filtering for battery management systems of LiPB-based HEV battery packs: Part 3. State and parameter estimation,'' J. Power Sources, vol. 134, no. 2, pp. 277–292, 2004.

[40] Allam, A., Onori, S., "An Interconnected Observer for Concurrent Estimation of Bulk and Surface Concentration in Cathode and Anode of a Lithium-ion Battery", *IEEE Transactions on Industrial Electronics*, pp. 7311 - 7321 Vol. 65, Issue: 9, 2018

[41] D. Di Domenico, A. Stefanopoulou, and G. Fiengo,''Lithium-ionbattery state of charge and critical surface charge estimation using an electrochem- ical model-based extended Kalman filter,'' J. Dyn. Syst., Meas., Control, vol. 132, no. 6, pp. 1–4, Nov. 2010.